International Journal of Greenhouse Gas Control 89 (2019) 9–19

Contents lists available at ScienceDirect

International Journal of Greenhouse Gas Control

journal homepage: www.elsevier.com/locate/ijggc

Experimental observations of CO_2-water-basaltic glass interaction in a large column reactor experiment at 50 °C

Deirdre E. Clark[a,*], Iwona M. Galeczka[b], Knud Dideriksen[c,1], Martin J. Voigt[a], Domenik Wolff-Boenisch[d], Sigurdur R. Gislason[a]

[a] Institute of Earth Sciences, University of Iceland, Reykjavík, Iceland
[b] Iceland GeoSurvey, Reykjavík, Iceland
[c] Geological Survey of Denmark & Greenland (GEUS), Copenhagen, Denmark
[d] Curtin University, Perth, Australia

ARTICLE INFO

Keywords:
Carbon sequestration
Fluid-rock interaction
Column reactor
CarbFix
Basalt glass
Basalt dissolution

ABSTRACT

Mineralization of water dissolved carbon dioxide injected into basaltic rocks occurs within two years in field-scale settings. Here we present the results from a CO_2-water-basaltic glass laboratory experiment conducted at 50 °C and 80 bar pressure in a Ti high-pressure column flow reactor. We explore the possible sequence of saturation with Fe-Mg-Ca-carbonate minerals versus Fe-Mg-clay and Ca-zeolite saturation states, which all compete for divalent cations and pore space during injection of CO_2 into basaltic rocks.

Pure water (initially with atmospheric CO_2) – basaltic glass reactions resulted in high pH (9–10) water saturated with respect to Mg-Fe-clays (saponites), Ca-zeolites, and Ca-carbonate. As CO_2-charged water (~20 mM) entered the column and mixed with the high pH water, all the Fe-Mg-Ca-carbonates became temporarily supersaturated along with clays and zeolites. Injected waters with dissolved CO_2 reached carbonate mineral saturation within 12 h of fluid-rock interaction. Once the pH of the outflow water stabilized below 6, siderite was the only thermodynamically stable carbonate throughout the injection period, although no physical evidence of its precipitation was found. When CO_2 injection stopped while continuing to inject pure water, pH rose rapidly in the outflow and all carbonates became undersaturated, whereas zeolites became more saturated and Mg-Fe-saponites supersaturated. Resuming CO_2 injection lowered the pH from > 8 to about 6, resulting in an undersaturation of the clays and Na-zeolites.

These results along with geochemical modelling underscore the importance of initial pCO_2 and pH values to obtain a balance between the formation of carbonates versus clays and zeolites. Moreover, modelling indicates that pauses in CO_2 injection while still injecting water can result in enhanced large molar volume Ca-Na-zeolite and Mg-Fe-clay formation that consumes pore space within the rocks.

1. Introduction

The CarbFix CO_2 storage pilot project in Iceland (Alfredsson et al., 2013; Aradóttir et al., 2012; Gislason et al., 2010; Matter et al., 2011; Khalibad et al., 2008; Oelkers et al., 2008) was established to investigate the potential of mineral carbon storage in basalt to reduce CO_2 concentration in the atmosphere. Conceptually, CO_2-saturated water enhances basalt dissolution due to their low pH, thus releasing primarily divalent cations into the solution. Stable carbonate minerals, such as calcite, magnesite, siderite, and mixtures thereof, then precipitate during the CO_2-water-basalt reactions (Daval, 2018; Gysi and Stefánsson, 2012a; Gysi, 2017; Kanakiya et al., 2017; Matter and Kelemen, 2009; McGrail et al., 2017; Schaef et al., 2010; Snæbjörnsdóttir et al., 2018; Xiong et al., 2017).

Carbon dioxide dissolved in water had mineralized within two years of field injection into reactive basaltic rocks at the CarbFix site in SW-Iceland (Matter et al., 2016; Snæbjörnsdóttir et al., 2017) and some of the supercritically injected CO_2 has also mineralized after two years at the Wallula Basalt Pilot Project in Washington, USA (McGrail et al., 2017). The rapid mineralization at the CarbFix site is attributed to the dissolution of CO_2 into water during injection, enhanced dissolution of the basaltic minerals and glass at low pH, as well as the mixing of the injected fluid with high pH groundwater that is further explored in this experiment (Snæbjörnsdóttir et al., 2017). Reaction path modelling of

* Corresponding author.
E-mail address: dec2@hi.is (D.E. Clark).
[1] Previous address: University of Copenhagen, Copenhagen, Denmark.

https://doi.org/10.1016/j.ijggc.2019.07.007
Received 24 January 2019; Received in revised form 7 June 2019; Accepted 8 July 2019
Available online 18 July 2019

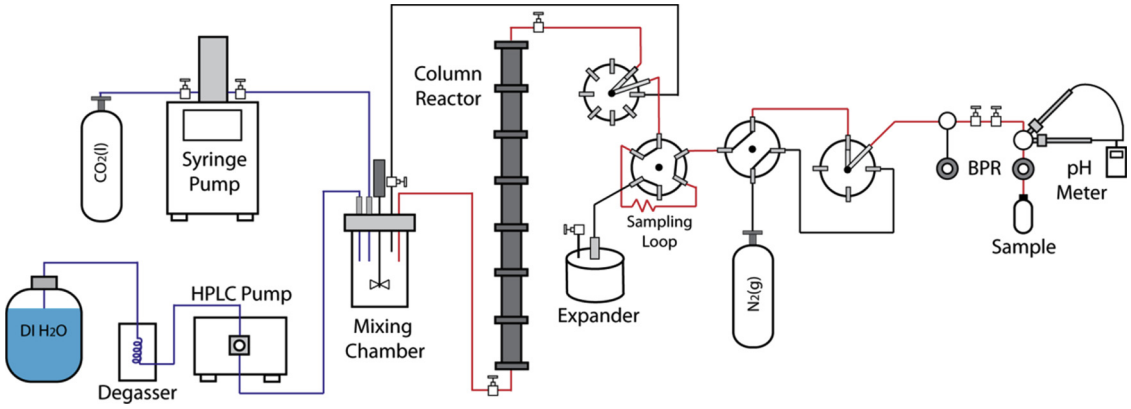

Fig. 1. Drawing of the experimental design, which is shown for both normal flow and the sampling mode. The CO_2 is mixed with H_2O and pumped through a 2.34 long column that is wrapped with heating tape. The inlet pathways are in blue. The reacted solution (in red) flows through a multi-position 8-port stream selector followed by a 2-position 6-port valve with a 5 mL sampling loop. Filtrated samples are collected once also passing a 2-position 4-port valve, a 4-port stream selector, a set of pH electrodes, and a back pressure regulator (BPR). The mixing chamber fluid can be sampled by changing the settings of the 8-port stream selector and closing off the valves to and from the column reactor (pathway in black). For more detailed descriptions and drawings of the various settings, refer to Galeczka et al. (2013).

the fluid in the first phase of pure CO_2 injection reveals that basaltic glass dissolution drives the mineralization of the bulk of the injected CO_2 along a slower, pervasive flow path, while a faster, high permeability flow path (the first breakthrough) is dominated by crystalline basalt dissolution. Modelling results of this first breakthrough (˜3% of the injected fluid) from the first monitoring well suggests that the initial carbon mineralization at the lowest pH (˜5) begins with siderite ($FeCO_3$), and as pH increases, mixtures of Fe-, Mg-, and Ca-carbonates take over; finally, at the highest pH, calcite is predicted to be the dominant alteration product (Snæbjörnsdóttir et al., 2018). This sequence had not been directly observed in the field as the pH was already too high (up to 8.2) in the first monitoring well with calcite being the final mineral product at pH > 8 (Snæbjörnsdóttir et al., 2017). Nevertheless, the modelled carbonate sequence is in agreement with (a) natural analogue studies (Rogers et al., 2006), (b) the observed well fluid chemical composition, and (c) the ^{14}C isotopic composition of the fluid within the first monitoring well (Matter et al., 2016). Additionally, the pilot project continued to inject water in between and after the two phases of gas injections and also had some operational complications to troubleshoot, leading to periods of discontinuous gas injection during the second phase of CO_2-H_2S-H_2 injection, which in turn resulted in pH fluctuations and elevated saturation states of secondary minerals like analcime and smectite (Gislason et al., 2018; Snæbjörnsdóttir et al., 2017).

Besides field test injections, numerous laboratory experiments have been conducted to examine sequestration of CO_2 within basalts by studying carbonation on basalt powders and grains (*e.g.* Gysi and Stefánsson, 2012a, 2012b; Hellevang et al., 2017; Rosenbauer et al., 2012; Schaef et al., 2010; Stockmann et al., 2011, 2013; Wolff-Boenisch and Galeczka, 2018) or basalt cores (*e.g.* Andreani et al., 2009; Adeoye et al., 2017; Kanakiya et al., 2017; Luhmann et al., 2017a, 2017b; Menefee et al., 2018; Xiong et al., 2017, 2018) as well as its inhibition by carbonate coatings and bacteria (*e.g.* Stockmann et al., 2012, 2014). From these studies, physical evidence of siderite, ankerite, and/or Mg-Fe-carbonates have been reported by Adeoye et al. (2017), Gysi and Stefánsson (2012a), Kanakiya et al. (2017), Menefee et al. (2018), Rosenbauer et al. (2012), Schaef et al. (2010), and Xiong et al. (2017). Of note is the residence time of these batch experiments, which lasted from a minimum of 12 days up to 182 days; this provides ample time for basalt dissolution and accumulation of enough divalent cations in the fluid to precipitate Fe-carbonates. Flow through experiments using basalt cores conducted by Andreani et al. (2009) identified minor amounts of siderite in a dead end fracture after a total run time of 450 min. On the other hand, a series of flow through experiments using basalt cores run by Luhmann et al. (2017b) for up to 33 days was unable to produce detectable siderite despite the saturation or supersaturation of the fluid with respect to siderite and reaction path modelling that had suggested siderite formation at low pH.

A 2.3 m long Ti high-pressure column flow reactor has been designed for CO_2-water-basalt experiments (Galeczka et al., 2013) to bridge the gap between field and laboratory-scale experiments. In addition to its large scale, this setup permits the sampling of a pressurized gas-charged liquid along a flow path and *in situ* monitoring of dissolved inorganic carbon and pH. The experiment described in this study utilized this column reactor but modified it with a high pressure syringe pump; this provided slower flow rates and increased residence times of the fluid within the column, thereby enabling longer water-rock interaction before the fluid exited the column. Galeczka et al. (2014) had previously conducted an experiment at 22 and 50 °C set at 22 bar pCO_2 aimed at studying CO_2-charged fluid-basalt interaction, however as the pH did not rise much above 4.5 after the first arrival of the CO_2-charged waters at 22 °C, saturation with carbonates (and precipitation) was unable to occur.

The aim of this experiment is to further investigate the proportions of injected dissolved CO_2 and high pH groundwater needed to reach a "sweet spot" in the reacted fluid composition that favors the saturation of carbonates rather than zeolites and clays at pH 5.2–6.5 (Snæbjörnsdóttir et al., 2018). In addition, this study explores the possible sequence of carbonate minerals' saturation states in the first phase of pure CO_2 injection of the CarbFix pilot project, and to study the consequences of discontinuous gas injection.

2. Materials and methods

2.1. Experimental design

This study used the Ti high-pressure column flow reactor (HPCFR) designed by Galeczka et al. (2013), where a detailed description can be found. One significant modification has been made to the setup; a high pressure syringe pump (VINCI Technology, BTSP-03-050) was used instead of a supercritical fluid pump to provide slower flow rates and longer residence times of fluids within the column, allowing for longer water-rock interaction. As depicted in Fig. 1, the syringe pump was connected to both a liquid CO_2 cylinder source and a 'mixing chamber' (mixed-flow-through Ti-Parr-reactor) with valves between each. The syringe compartment was first filled to its capacity with CO_2(l). Once filled and the valve closed off from the cylinder, the volume of the syringe was adjusted to obtain a pressure of ˜80 bar. Subsequently, the valve between the 'mixing chamber' and syringe pump was opened so that the liquid CO_2 was allowed to mix with the degassed deionized (DI)

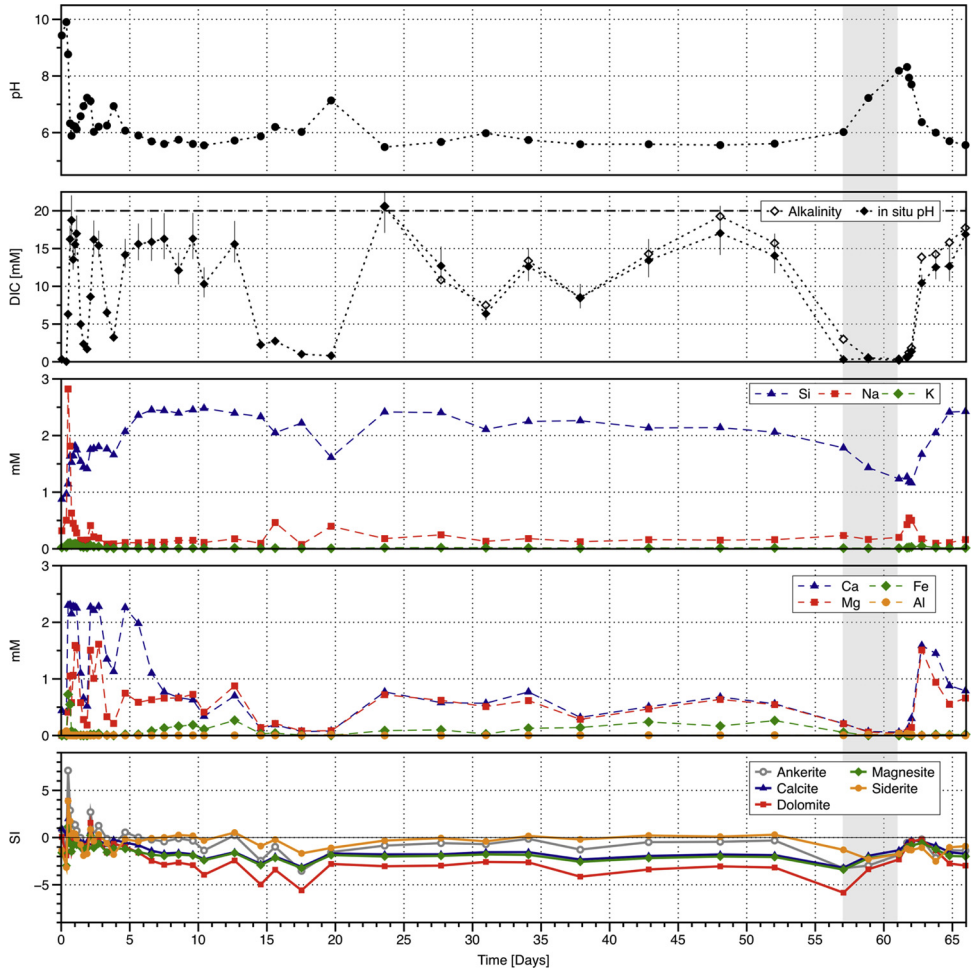

Fig. 2. Outlet pH, DIC, major element concentrations, and mineral saturation indices (SI) of carbonates during the 66 days of experimental duration. The light gray shaded area represents the approximate 100 h when the syringe pump failed and no new CO_2 entered into the 'mixing chamber'. Error bars for DIC concentrations were calculated from only varying pH ± 0.10. The dotted line represents the input DIC.

water (18.2 MΩ × cm^{-1}) delivered by a high pressure liquid chromatography pump (HPLC). The stirring rate in the mixing chamber was 300 rpm and the average residence time of the CO_2-water mixture within the 100 mL chamber was ~30 min to assure full dissolution. The CO_2-charged water from the 'mixing chamber' was pumped through the column filled with basaltic glass powder (see Section 2.2). This starting solution could also be sampled when closing off the valve between the mixing chamber and the column reactor, thereby bypassing the reactor. This column measured 234 cm in length, 5.0 cm in inner diameter, and held a total volume of 4.78 L.

Initial conditions were set to be similar to that of the CarbFix pilot project (Sigfusson et al., 2015; Matter et al., 2016; Snæbjörnsdóttir et al., 2017). As groundwater temperatures at the field site ranged from 20 to 50 °C, the experiment was set to 50 ± 0.5 °C using heating tape. The starting *in situ* pH of the flowing fluid in the filled column before CO_2 injection was 9.8, which was analogous to the area's groundwater pre-injection where the pH ranged from 8.9 to 9.8 (Alfredsson et al., 2013) as a result of DI water-rock interaction. The experiment CO_2(l) and water pump flow rates were fixed to 0.004 and 3.5 mL/min, respectively, giving an average fluid residence time of 12 h in the column. Based on these rates, the dissolved inorganic carbon (DIC) concentration and pH of the CO_2-charged inlet fluid were ~20 mM (mmol/kg water) and ~4.0, respectively. For comparison, the DIC and pH in the CarbFix injection well were 823 mM and 3.85, respectively (Sigfusson et al., 2015). The lower pCO_2 (0.60 bar) in the laboratory experiment would limit the formation of zeolites and clays, but still promote carbonate formation as the expected pH was computed to be within the "sweet spot" of 5.2 to 6.5 (Snæbjörnsdóttir et al., 2018).

2.2. Material

Stapafell basaltic glass was used as the filling material for the column, which originated from the Stapafell Mountain located in SW Iceland. This material has been widely used and characterized in previous experiments on glass dissolution kinetics (Galeczka et al., 2014; Gysi et al., 2012a; 2012b; Gudbrandsson et al., 2011; Gislason and Oelkers, 2003; Oelkers and Gislason, 2001; Stockmann et al., 2011; Wolff-Boenisch et al., 2011). Its major element chemical composition, normalized to one Si atom, was $Si_{1.000}Ti_{0.024}Al_{0.358}Fe_{0.188}Mg_{0.281}Ca_{0.264}Na_{0.079}K_{0.008}O_{3.370}$ (Oelkers and Gislason, 2001). The material preparation procedure can be found in the Supplementary Material.

The BET specific surface area (A_{BET}) before the experiment was 1240 cm^2/g, as measured by six-point N_2 adsorption using a Quantachrome Gas Sorption system, and the specific geometric surface area (A_{geo}) calculated was 286 cm^2/g, assuming the glass powder to be composed of identical cubes and based on the particle density and equations reported by Wolff-Boenisch et al. (2006). The total BET surface area in the column amounted thus to 8,358,000 cm^2 and the corresponding geometric surface area was 1,927,000 cm^2, yielding a geometric surface area to solution volume ratio of 760 cm^{-1}. The difference in BET surface area compared to previous experiments using

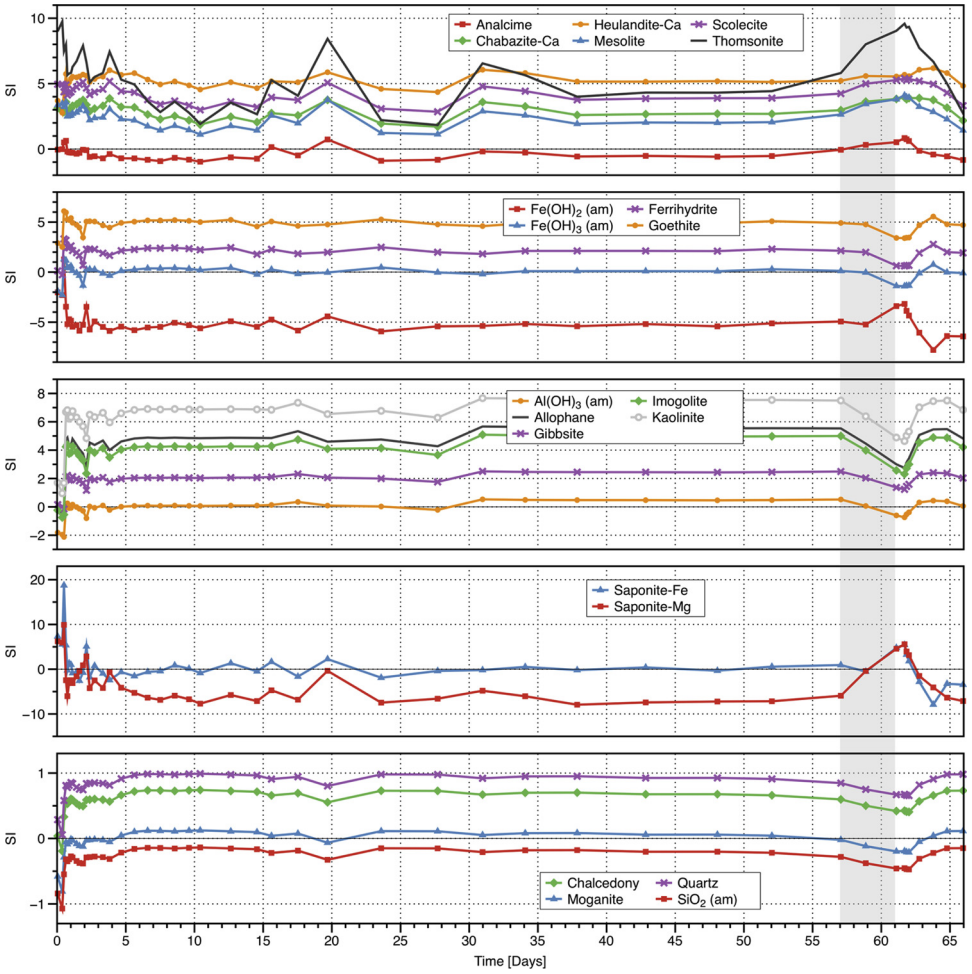

Fig. 3. Mineral saturation states of zeolites, Fe-oxides, Al-oxides, clay minerals, and silica phases during the experiment after 66 days. The light gray shaded area represents the approximate 100 h when the syringe pump failed and no new CO_2 entered the 'mixing chamber'.

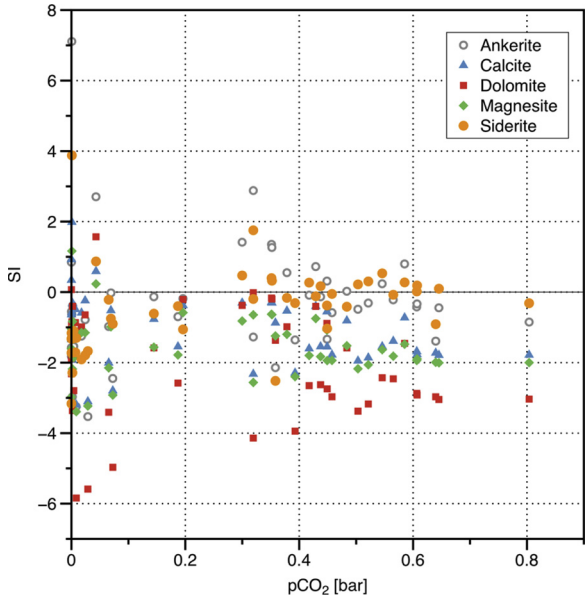

Fig. 4. Mineral saturation indices of carbonates against pCO_2 during the experiment.

Stapafell basaltic glass can most likely be attributed to different particle size distributions and surface roughness (Wolff-Boenisch et al., 2016). It is most similar to the Stapafell glass of Stockmann et al. (2011) and Wolff-Boenisch et al. (2011), which has a A_{BET} of 5880 cm^2/g.

2.3. Analysis

To chemically characterize the H_2O-CO_2 system, pH was measured in-line at the outlet of the column (Fig. 1) using high pressure temperature stainless steel pH electrodes (Corr instruments, Texas) with a precision of ± 0.1 pH unit. The pH electrodes were calibrated at the start, during, and end of the experiment. DIC was recalculated using the measured *in situ* pH and concentrations of the major elements excluding carbon, assuming charge balance, or from the alkalinity, which started to be measured after 20 days of experiment duration. The geochemical modelling software, PHREEQC (Parkhurst and Appelo, 1999), was used for these calculations, further described in Section 2.4.

Fluids were sampled from the outlet of the column (Fig. 1) for analysis of their major elemental composition by inductively-coupled plasma optical emission spectrometry (ICP-OES) and ion chromatography. After the completion of the experiment, the solid material was analyzed by scanning electron microscopy (SEM), X-ray diffraction (XRD), and X-ray photo electron spectroscopy (XPS). A detailed description of the fluid sample analysis along with the procedures for preparation and analysis of the solid material is located in the Supplementary Material.

Many techniques exist for characterizing solids and the changes to

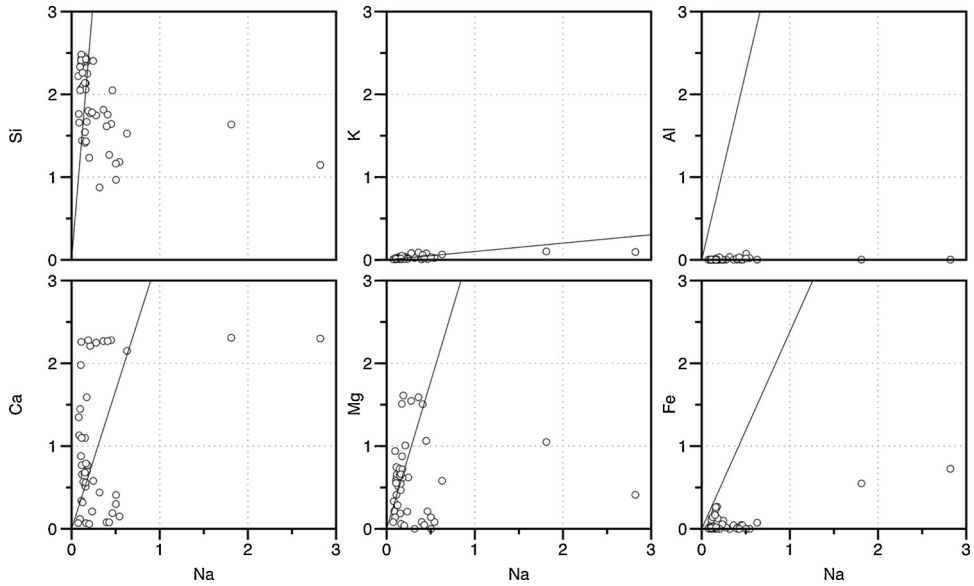

Fig. 5. Element mobility relative to Na. Values plotted on the line represent stoichiometric dissolution of basaltic glass whereas values to the right indicate secondary mineral formation.

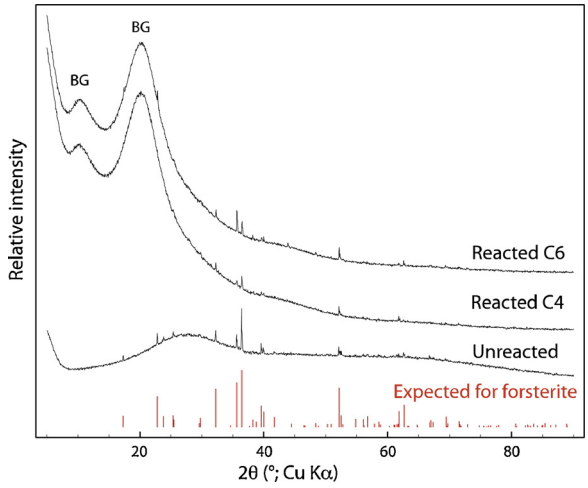

Fig. 6. XRD of the unreacted Stapafell basaltic glass and samples from compartments 4 (C4) and 6 (C6) after 108 days of reaction. Red bars indicate peaks expected for forsterite based on Birle et al. (1968).

them that occur during water-mineral interaction. Some, such as computed tomography, are able to probe large volumes, but suffer from poor spatial resolution; others, such as transmission electron microscopy of thin foils cut with a focused ion beam, have outstanding spatial resolution, but probes only extremely small volumes of sample. As a compromise between investigated volume and spatial resolution, the suite of techniques employed probes relatively large portions of samples and provides information on structure within larger volumes of samples. However, XRD is unlikely to detect changes affecting only small volumes of material at the grain surface. XPS is highly surface sensitive, yielding information on the composition of the top 10 nm of materials. This technique is particularly useful for detection of thin surface coatings, and an area ~300 μm by ~700 μm of the packed sample is irradiated during analysis. Finally, through repeated EDXS mapping and SEM imaging at variable magnification, the composition at an area of approximately 250 μm by 250 μm was probed. The spatial resolution of EDXS at our operating conditions means that significant compositional variation can be detected only with ~1 μm resolution or so in all three dimensions. Thus, thin surface coatings will be unseen, but even fairly rare occurrences of micrometre sized particles or aggregates with highly contrasting chemical composition should be identifiable (*e.g.* carbonate minerals on top of the basaltic glass).

2.4. Geochemical calculations & modelling

Aqueous speciation, mineral saturation states, and reactive transport modelling were performed using the PHREEQC 3.4.0 geochemical code (Parkhurst and Appelo, 2013) and the *carbfix.dat* database (Voigt et al., 2018), which is based on the *core10.dat* database (Neveu et al., 2017); relevant mineral phases and further additions are listed in Table S-1.

For aqueous speciation and mineral saturation index (SI, defined as the base-10 logarithm of the saturation state, which is the ratio of the ion activity product to the equilibrium constant of the precipitation reaction) calculations, chemical compositions of the sampled fluid together with pH measured in-line (corrected to the experimental temperature) at the outlet were used. As described earlier, PHREEQC calculations based on pH, measured concentrations, and charge balance constraints were performed to estimate DIC concentrations used for further calculations, which were then verified with corresponding alkalinity measurements and no charge balance constraint. Aqueous speciation and saturation state calculations used measured Fe^{II} and Fe^{III} concentrations as redox indicators for the CO_2-charged water experiments.

The fluid chemistry in the reactor was modelled using a one-dimensional reactive transport simulation with seven cells, similar to that of Galeczka et al. (2014). The advective flow of the fluid was simulated in PHREEQC by moving the reactive fluids to the subsequent cell after each time step, which corresponded to its residence time within each cell. The fluid phase was allowed to react with basaltic glass, whose dissolution rate was taken from Gislason and Oelkers (2003) and assumed to dissolve stoichiometrically. The basaltic glass surface area used in the model was set to approximately one-tenth of the A_{geo}, like that of simulations run by Aradóttir et al. (2012), Beckingham et al. (2016, 2017), Galeczka et al. (2014), and Gysi and Stefánsson (2012a). The Fe redox state of the fluid was effectively controlled by the amounts of Fe^{II} and Fe^{III} released from the basaltic glass and then taken up by secondary minerals. Several mineral phases were allowed to precipitate by constraining them to local equilibrium with the fluid (*i.e.* assuming fast precipitation kinetics relative to fluid residence times) based on

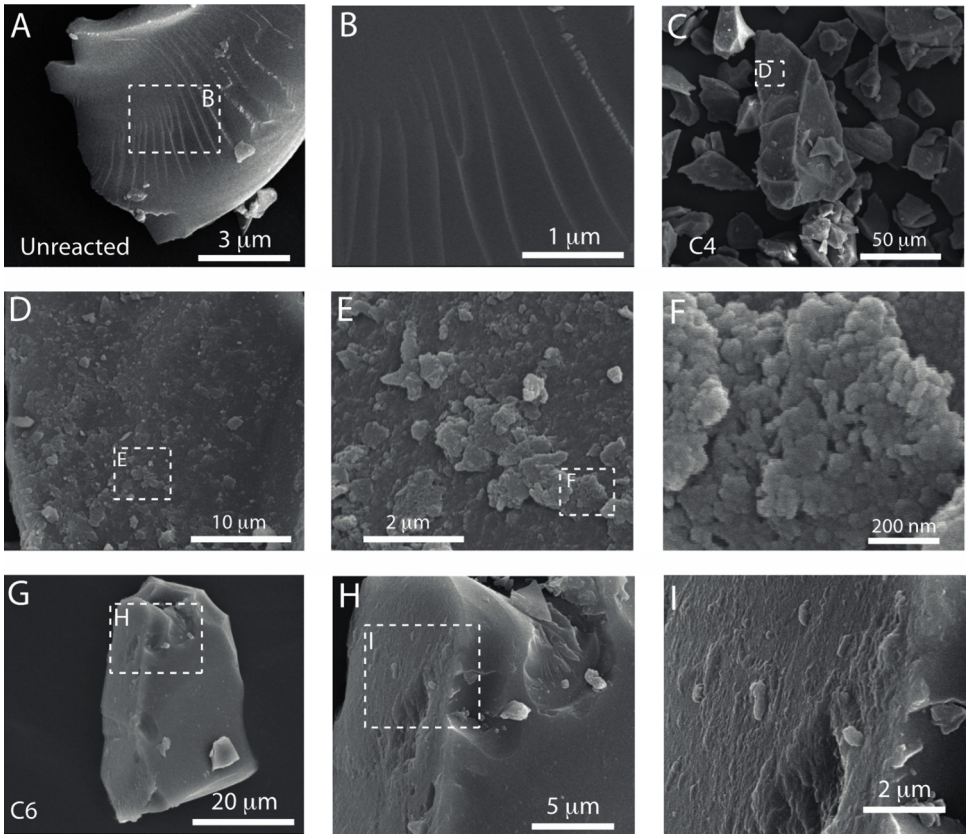

Fig. 7. SEM of unreacted Stapafell basaltic glass (A and B), of sample from compartments 4 (C4; C–F) and 6 (C6; G–I)) after 108 days of reaction.

experimental results and common secondary minerals found in natural basaltic systems (Alfredsson et al., 2013; Rogers et al., 2006).

3. Results

In the beginning of the experiment, high pH pore water (9.8) resulted from a continuous flow of DI water deprived of CO_2 through the column of basaltic glass grains, followed by a CO_2-water injection at a pCO_2 of 0.60 bar, or 20 mM, for 108 days, of which 66 days (132 pore volumes) are discussed here. Stagnation of the CO_2-charged fluids within the HPCFR occurred several times in the latter half of the experiment due to refilling of CO_2 in the syringe pump, the HPLC pump stopping, or the sampling of compartments along the column (of which a detailed description can be found in Galeczka et al., 2013). The resulting disturbances to the pH and DIC thus altered the steady state behavior of several mineral saturation states.

Each sample taken from the outlet represents water-rock interaction during the 12 -h passage through the column reactor. This experimental setup simulates sampling of the injected fluid from a single monitoring well downstream from an injection well, where each water sample represents a single passage between the injection and monitoring well. See Table S-2 for the chemical compositions of the fluid samples.

3.1. Outlet fluid chemistry

Measured outlet pH, major element concentrations, calculated DIC, and mineral saturation states during the experimental runtime of 66 days are shown in Figs. 2 and 3, with a more detailed evolution of the outlet fluid compositions during the first 13 days shown in Fig. S-1 (Supplementary Material). Within 18 h of the initial CO_2 injection and 1.5 PV of CO_2-fluid-rock interaction, the pH decreased from 10 (resulting from the initial DI water-basalt interaction) to 6–6.5 while DIC increased and briefly reached the 20 mM inlet concentration (Fig. 2). This simulates the mixing of injected fluid with high pH groundwater during field injections. All major elements increased in concentration within 1–2 PV, with the exception of Al and K. All the Ca-Mg-Fe-carbonates became supersaturated with respect to the pore fluids around pH 8.8 with the first arrival of the CO_2-charged water after 12 h of interactions.

The pH was mostly stable at ~5.6 from days 4 to 52 while DIC fluctuated. Concentrations of major elements stabilized after four days, while Ca and Mg stabilized after six days. Siderite was at or slightly above saturation and the other carbonates undersaturated until day 53. The majority of total dissolved Fe was also observed as Fe^{II} rather than Fe^{III} (Fig. S-2).

After approximately 56 days, the syringe pump failed for an estimated 100 h and no new CO_2 entered the 'mixing chamber' and thereby only DI water was pumped through the column from the HPLC (Fig. 1). This mimics the geochemical consequences of alternating water and CO_2-charged water injections during field-scale carbon capture and storage. It took about 10 PV (5 days) for the pH to peak at 8.7. During this time, carbonate mineral saturation indices and major element concentrations changed with a slight delay, with a significant undersaturation with respect to siderite and decreased concentrations of aqueous Si, Ca, and Mg concentrations.

Once the pump was running again (day 61), it took 6 PV (3 days) for the outlet pH to restabilize at ~5.7 and the DIC to increase. In response, outlet concentrations of all elements, besides K, Al, and Fe, also increased and returned to previous levels once the pH re-stabilized.

Changes in mineral saturation indices for zeolites (Fig. 3) reflected the changes in dissolved constituents and the composition of the zeolites, for instance the fluid was reaching saturation with respect to the Na-zeolite (analcime) only when the pH was above 7. The clay minerals, Fe-saponite and Mg-saponite ($Fe/Mg_{3.175}Al_{0.35}Si_{3.65}O_{10}(OH)_2$), very common alteration minerals in basaltic terrain at low temperature < 100 °C (Alfredsson et al., 2013; Schiffman and Fridleifsson,

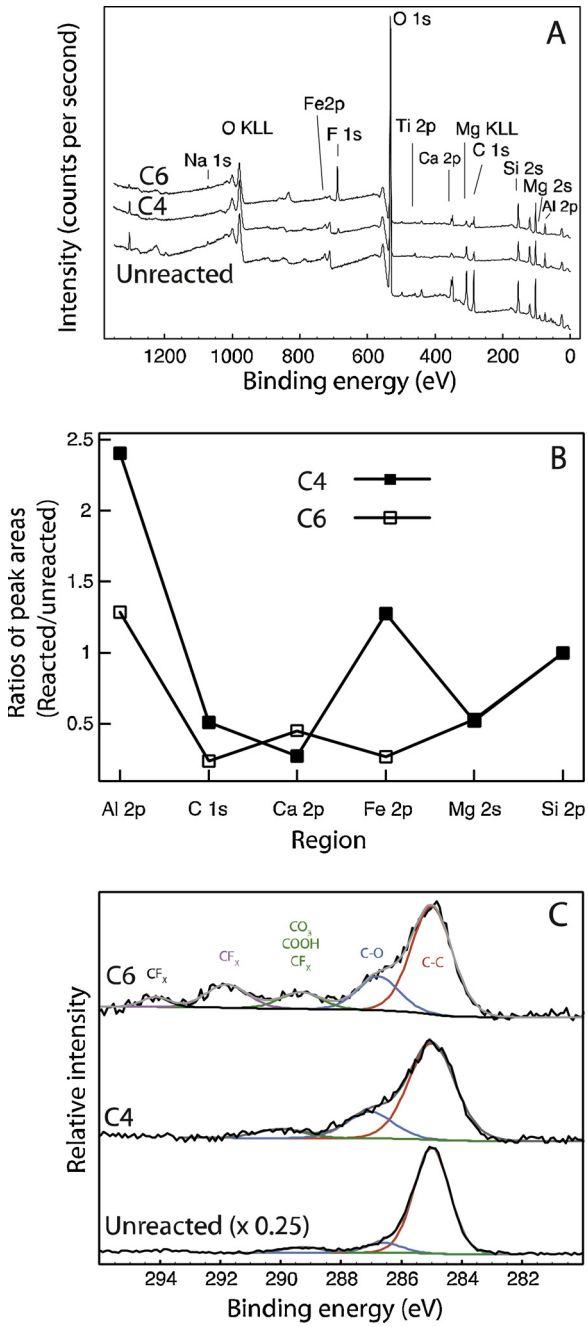

Fig. 8. XPS of the unreacted and reacted Stapafell basaltic glass from compartments 4 and 6 (C4 and C6): (A) survey scan, (B) ratios between the integrated numbers of counts of unreacted and reacted material normalized to those for Si, and (C) detail scan for C1s.

1991), also reached supersaturation only when pH was higher than 7, with Fe-saponite mostly at saturation. The fluids were supersaturated with respect to most of the Fe-oxides, Al-oxides, and silica phases for the duration of the experiment. All minerals reflected major changes in pH and DIC concentrations.

The relationship between pCO_2 and the saturation states of carbonate minerals in Fig. 4 depicts the supersaturation of siderite and ankerite when pCO_2 values were between 0.3 and 0.7 bar with the highest saturation levels between 0.3 and 0.4 bar. Note that the supersaturation of all carbonate minerals at pCO_2 of < 0.05 bar occurred during the initial arrival of CO_2-charged fluids.

Na was chosen as a reference element to evaluate element mobility because it was considered the closest representation of a mobile element under the present experimental conditions, though it should be noted that some Na might have been incorporated into secondary minerals. The results are shown in Fig. 5 relative to the stoichiometry of the Stapafell basaltic glass. Aluminum and Fe indicate either non-stoichiometric dissolution and/or precipitation into secondary minerals. The latter was expected considering the saturation or supersaturation of various Al minerals, clay minerals, zeolites, and siderite (Figs. 2 and 3). Potassium showed the opposite behavior by dissolving stoichiometrically relative to Na, independent of any changes in DIC. There was both stoichiometric and non-stoichiometric dissolution of the divalent cations, Ca and Mg, as well as Si, reflecting experimental changes in pH leading to the formation of relevant secondary minerals. The greatest element mobility occurred during the initial arrival of the CO_2-charged waters within the column after 1 PV.

3.2. Solid chemistry

XRD of the unreacted material shows a broad background centered at about 30° 2θ as well as smaller peaks for forsterite (Fig. 6). Apart from two broad peaks from the dome protecting the sample from oxidation, only the peaks from forsterite were discernible for the reacted material. Thus, crystalline secondary phases were not present in amounts allowing detection with XRD (> 0.5% or so).

SEM of the initial material often shows < 50 nm protrusions on the glass surface. At times, these adorn conchoidal fractures, indicating that they formed after the crushing of the material (Fig. 7A). Presumably they have formed as a result of reactions occurring during the washing of the material prior to use and/or from reaction mediated by the thin water layer covering ionic compounds in air. After reaction with CO_2-charged water, the surfaces appeared more altered, in particular for material from compartment 4 (C4), where the original glass surface often cannot be discerned (Fig. 7D–F; more images in Supplementary Material). Here, the surface region was composed dominantly of ~40 nm spherical or semi-spherical particles, whose exact morphology cannot be determined because of the spatial resolution and the presence of a ~10 nm gold coating. Often such particles appeared organized in flakes (Fig. 7E–F). In addition, platy particles with variable widths, sometimes reaching > 1 um, were common in the images. Overall, the topographical relief had increased significantly because of spatially uneven dissolution and/or secondary phase formation. During the imaging, we conducted ~20 EDXS spot analysis of particles, whose morphology might resemble siderite, chukanovite, or amorphous iron carbonate, and made ~20 maps to probe larger areas for abnormal concentrations of Ca, Mg, Fe, C, and Si. Neither of the datasets showed signs that could be attributable to carbonates. Thus, we conclude that carbonate minerals did not occur as single or aggregated particles with dimensions large enough for EDXS detection (~1 um with the settings used).

XPS survey scan of the unreacted materials contains peaks for O, Si, Mg, Ca, Fe, Ti, Na, and C (Fig. 8A). After reaction, peak intensity decreased significantly for Na, Ca, and Mg, and to lesser degree for Si and Mg. In contrast, peaks for Fe were similar in intensity and the peak for Al was more pronounced. For the sample from compartment 6 (C6), the intensities of the Fe peaks were significantly lowered. Fig. 8B shows the integrated peak area quantified from detail scans as ratios between the values determined for the reacted material divided by those for the unreacted material and normalized to the counts for Si. For Al, the ratio was well above 1, indicating its surface enrichment compared to Si. In contrast, Ca and Mg showed low ratios, signifying significant depletion. For Fe, ratios were similar for the unreacted material and the sample from C4, whereas the sample from C6 revealed significant depletion in Fe compared to Si. Inspection of the detailed scan for the Fe 2p region (Fig. S-3) shows that little difference exists between the spectra for the unreacted material and the sample from C4, indicating that little change occurred in the Fe surface concentration and its valency as a result of reaction. For C6, the low Fe concentration complicated determination of Fe valency.

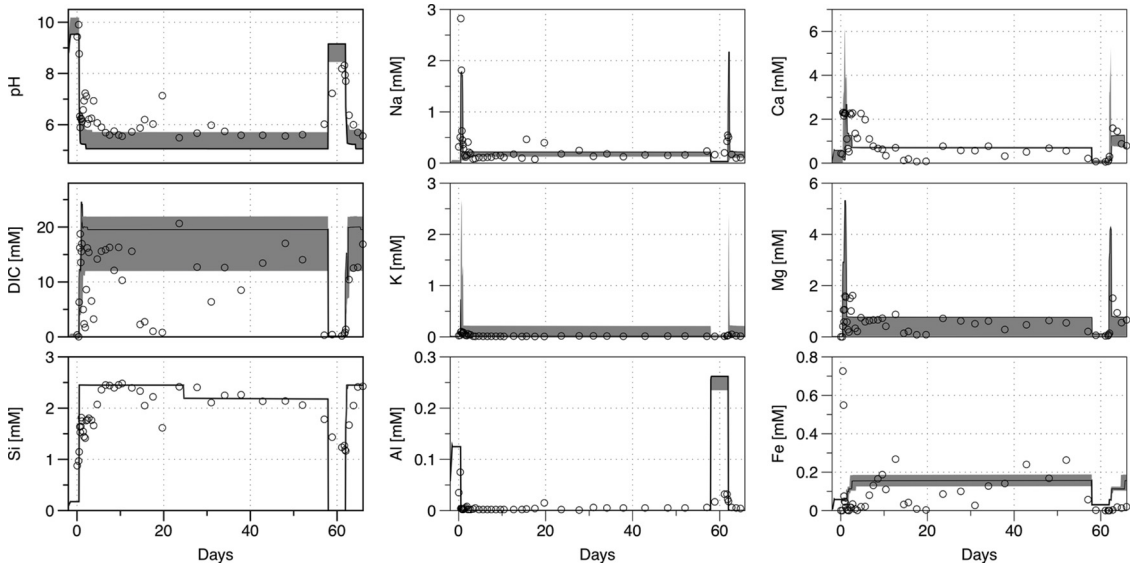

Fig. 9. Comparison of reactive transport modelling results (black line) with measured experimental outlet fluid concentrations (open circles). The gray shaded area represents the effect of a variability of 15–25 mM in input DIC concentrations.

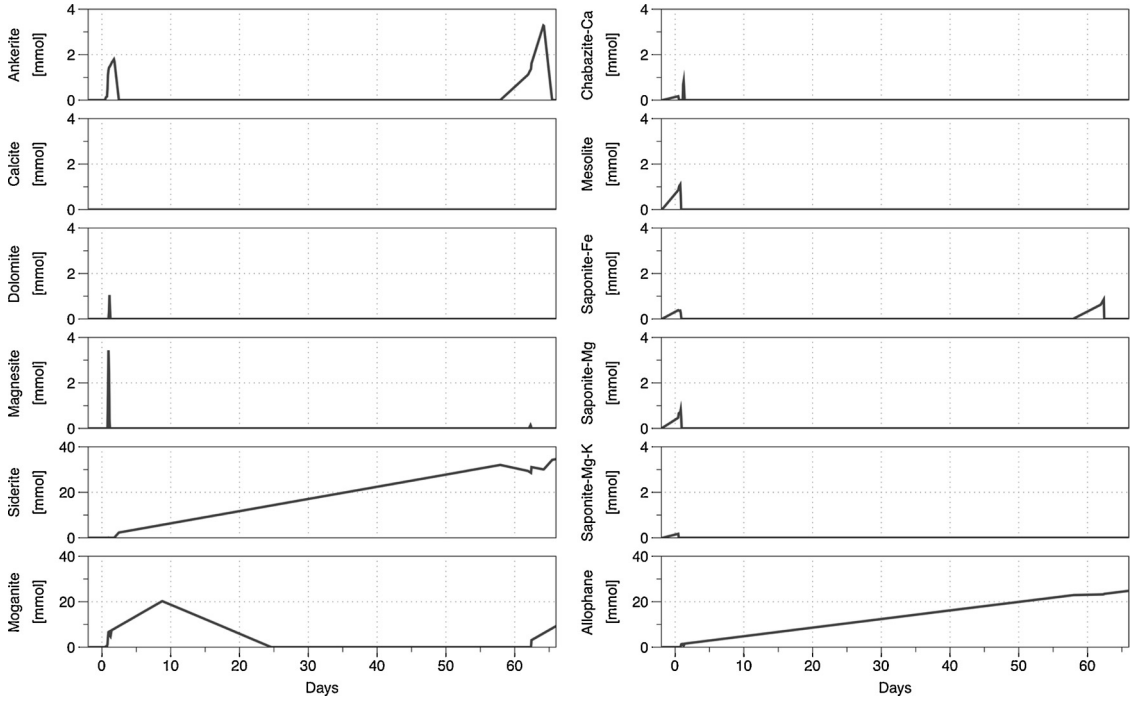

Fig. 10. Cumulative amount (millimoles) of selected minerals allowed to precipitate in the reactive transport model. Note the variable scale on the y-axis.

During reaction, the overall peak intensity decreased significantly for carbon. The detail scan for C1s had been fitted with three or more components (Fig. 8C). The component at low binding energy was assumed to represent adventitious carbon. This peak had been assigned a value of 285 eV in the calibration of all spectra. The component at the slightly higher binding energy most likely represented C–O bonds, whereas the small component at binding energy of ˜290 eV may be attributable to carboxylate groups or carbonates. Thus, XPS provides no evidence for carbonate phases existing commonly as surface coatings or more evenly distributed, small particles, which would have gone unnoticed in EDXS. Based on this data, we conclude that carbonate solids occurred only very rarely, if at all, in the sampled material after 108 days of reaction. However, the data indicate that Fe was not leached to the same degree as other divalent cations from the central part of the column.

3.3. Reactive transport modelling

In the 1D reactive transport model to simulate the experiment, CO_2 addition to the water flowing through the basaltic glass system was active for 57 days, or 114 PV, stopped for four days (8 PV), and then active again for an additional five days (10 PV), making a total of 66 days. Many phases in the fluid phase were supersaturated during the experiment (Fig. 3), therefore several were allowed to precipitate at local equilibrium in the model: moganite, allophane, Mg- and Fe-saponites, Ca-chabazite, and mesolite in addition to the carbonate minerals – ankerite, calcite, dolomite, magnesite, and siderite. It was found that reducing the geometric surface area of the basaltic glass in

the model to approximately one tenth of that estimated from the mass of basalt used in the experiment resulted in a good agreement of modelled major elemental concentrations in the outlet fluids in comparison with the corresponding experimental data. Furthermore, moganite's saturation index was adjusted to 0.1 to better reflect the experimental results shown in Fig. 3. The results of the simulations were compared to the experimental results (Fig. 2) in Fig. 9.

Predicted pH, DIC, and major element concentrations are generally comparable to that of the experimental results (Fig. 9); modelled results were within or close to the range of measured values before the addition of CO_2. When 20 mM of CO_2 was added to the simulation, results showed peaks in Ca, Mg, and Na in addition to the increased concentrations of DIC, Si, and Fe and decreased pH and Al values, similar to the experimental data. During the simulated stop of CO_2 addition, the modelled results reflected the changes in expected increased or decreased concentrations, with the exception of K, Na, and a small peak in Fe. By varying the amount of CO_2 added to the simulation from 15 to 25 mM, the changes to the modelled major element chemistry were minimal with the expected exception of DIC, which shows a variation similar to that in the experiments, suggesting that injected CO_2 may have varied within these limits.

According to the reactive transport model, the initial arrival of CO_2 (1–2 PV) would enable ankerite, dolomite, and magnesite precipitation, though this was soon taken over by siderite and rapidly forming Al/Si phases (moganite and allophane in this model, Fig. 10). After 57 days, around 5750 mmols of CO_2 had been injected into the system, while only 32 mmols of siderite was predicted to have been precipitated (less than 1% of the injected CO_2). When no new CO_2 was added after this, allophane and siderite began to slowly dissolve and ankerite and Fe-saponite started precipitating. However, as soon as CO_2 re-entered the system, ankerite rapidly precipitated and re-dissolved, magnesite briefly formed while allophane, moganite, and siderite all started to precipitate again. With this second "plume" of CO_2-charged fluids, only ankerite and siderite were able to precipitate, ankerite for at least 1 PV with siderite continuing to form as before. Due to its relatively large molar volume, the allophane predicted to form has by far the largest cumulative volume, as shown in Fig. S-4, followed by siderite and moganite.

4. Discussion

Both the immediate change in pH and subsequent supersaturation of carbonates were previously noted during the first arrival of CO_2-charged waters at the CarbFix field injection site (Snæbjörnsdóttir et al., 2017) and preceding HPCFR experiments (Galeczka et al., 2014). These cases did have significantly higher injected DIC concentrations of 823 and 300 mM, respectively, compared to this experiment. Siderite was the first carbonate mineral to become saturated at the lowest pH during the first phase of the CarbFix field injection of pure CO_2, and the monitoring solutions remained supersaturated with respect to siderite and ankerite weeks after the injection was stopped. Furthermore, calcite was oversaturated before injection and was a common alteration mineral in the subsurface rocks, but became undersaturated after days of injection (Alfredsson et al., 2013; Snæbjörnsdóttir et al., 2017). Calcite and dolomite reached supersaturation several days after injection and remained so to the end of the monitoring close to 600 days after the initial CarbFix injection (Snæbjörnsdóttir et al., 2017). Furthermore, Mg-saponite, a smectite, was oversaturated in all samples, except for the samples taken during and shortly after the two CarbFix injections where pH was < 8 (Snæbjörnsdóttir et al., 2017). Smectite is one of the most abundant secondary minerals in basaltic rocks at < 100 °C and had been identified in all wells drilled at the CarbFix site in Hellisheiði, SW-Iceland (*e.g.* Schiffman and Fridleifsson, 1991).

This sequence of carbonate and Mg-saponite saturation stages was explored in the present study by lowering the injected DIC concentration to 20 mM, forty-fold more dilute than the injected DIC concentration in the pure CO_2 injection phase of the CarbFix pilot study, considered the "sweet spot" for carbonation (Snæbjörnsdóttir et al., 2018). This was necessary because of the short reaction time (12 h) within the HPCFR. The sequence of carbonation varied throughout the experimental run, as shown in Figs. 2 and S-1. The rapid rise in Ca and Mg concentrations at the start of the experiment suggests that high pH mineral phases, like calcite, Mg-saponite, and Ca-zeolites, had previously formed before the addition of CO_2 and were immediately dissolving. This is supported by the supersaturation of these minerals during the first day (Figs. 2–3). In addition, the quick dissolution of calcite during the first four days would clarify Ca's deviation from stoichiometric dissolution observed in Fig. 5. At the lowest pH (30–45 days), siderite was at saturation followed by, in sequence of lowest to highest undersaturation, ankerite, calcite, magnesite, and dolomite. When CO_2 injection stopped after 57 days, the sequence changed, not only dictated by pH and pCO_2, but by the relative activity of the Fe, Mg, and Ca dissolved species (Fig. 2). Once pH stabilized below 6, Mg-saponite was undersaturated throughout the CO_2 injection (Fig. 3), and after the CO_2 injection was terminated, Mg-saponite became supersaturated. This mimics the first phase of the CarbFix field injection, as described above.

Despite the thermodynamic stability of siderite for at least 24 days, based on mass balance calculations approximately 45–70 cm^3 of siderite (2–3% of the total material) could have precipitated, but in this case 25–50 cm^3 of it would have re-dissolved before the pump failure as siderite never went much above saturation. Its complete dissolution would have been ensured when the syringe pump failed and afterwards. This is in agreement with the lack of Fe-carbonates among the detected alteration products on the surfaces of the basaltic grains; energy dispersive X-ray spectroscopy was unable to determine compositions of any potential alteration product from the thin alteration layer. Conceivably if the saturation indices of siderite and ankerite had been higher (> 1), homogenous nucleation could likely occur as opposed to surface-controlled growth, as observed from the calcite precipitation experiments conducted by Stockmann et al. (2014). This, in turn, could provide the seeds, or nuclei, for further surface-controlled growth of carbonates at lower saturation levels provided that the pH is not too low, in which case carbonates would re-dissolve. However, this study demonstrates that already at pH 5.7 most of the carbonates become undersaturated. Yet, if pH is > 7, then Fe- and Mg-saponites become oversaturated with many zeolites always saturated, especially when pH is higher than 6. Consequently, this reveals an even narrower "sweet spot" for efficient carbonation than the suggested 5.2 to 6.5 (Snæbjörnsdóttir et al., 2018).

Reactive transport modelling of the experimental conditions provided insight to the possible mineral groups competing for the divalent cations. Fe-rich saponite, rather than iron oxides, was competing with siderite for Fe^{II}, which was similarly observed for Mg between Mg-rich carbonates and saponite (Fig. 10). On the other hand, Ca-rich zeolites like chabazite would have been competing for Ca with calcite instead of clays. However, there was little competition between the carbonates and the clays/zeolites when CO_2 injection was occurring (Fig. 10) due to the fluids being undersaturated with Ca-carbonates. Most likely the formation of Al/Si-containing solids like allophane and moganite prevented the precipitation of any zeolites due to the limited availability of Si and Al and their relative thermodynamic stabilities at low pH. Notably though, only a few carbonates besides siderite were predicted to briefly precipitate with each arrival of new CO_2 to the water-basaltic glass system, while siderite was able to form during the entire CO_2 injection time.

While inadvertent, important observations were made when the syringe pump for CO_2 failed, especially as discontinuous injections will always occur at the industrial-scale (Gislason et al., 2018). The discontinuous injection was characterized by a rapid increase in pH and decrease in DIC (similar to the trends seen during CarbFix after the injection of pure CO_2 in March 2012; Matter et al., 2016), which in turn

suggests that a brief failure of the pump transpired around days 15–20 (Fig. 2). In addition, the pump failure in the experiment led to prompt changes in mineral saturation states, particularly the supersaturation with respect to clays/zeolites like Mg/Fe-saponites, analcime, and thomsonite as well as the decrease in saturation with respect to the carbonates. This was also observed during CarbFix during the two month period between the pure CO_2 and the gas mixture injections, where only water was injected; a perfect example to observe the natural state of the fluids reacting with the basaltic rocks (Snæbjörnsdóttir et al., 2017). Based on these field observations, in the event of a gas injection stoppage in the field, for example due to routine maintenance, it is important to note that the injected water would still have some alkalinity. This lack of alkalinity in the DI water injected in the experiment had led to immediate undersaturation of all carbonates, which would not be the case in the field. However, during long periods of no gas injection, the stability fields of saponites and zeolites would change to favor their precipitation, thereby consuming valuable pore space for carbonates. Further research on a site-by-site basis will be necessary to anticipate any potential complications for this scenario in addition to a complete shutoff of gas and water injection.

These experimental results, as well as results from the subsequent reactive transport model, demonstrate how sensitive the fluid chemistry and mineralization are to any abrupt changes in pCO_2 input. The sensitivity of calculated DIC concentrations to uncertainties in measurements also highlights the challenge of monitoring the injected fluid chemistry during experiments when changes in DIC between the inlet and outlet are small. One suggestion to further improve the precision is to include another set of pH probes in-line, between the mixing chamber and the column, thereby allowing to calculate injected DIC (Rendel et al., 2018). However, it is important to note that inferred DIC concentrations are sensitive to uncertainties in such pH measurements.

5. Conclusions

Water dissolved CO_2 was injected into a 234 cm long titanium HPCFR at 50 °C and 80 bar pressure that was already filled with basaltic glass grains and DI-water. The experimental outlet fluids reached carbonate mineral saturation within 12 h of fluid-rock interaction.

As the CO_2-charged water (˜20 mM) entered the column and mixed with the high pH water (9–10), the outlet fluid with respect to Fe-, Mg-, and Ca-carbonates all became temporarily supersaturated along with clays and zeolites. Once the pH of the outflow water stabilized below 6, siderite ($FeCO_3$) was the only stable carbonate along with Fe-, Al-, and Si- oxides and hydroxides, Fe-saponite, and Ca-zeolites. When CO_2 injection was terminated while continuing to inject pure water, pH rose rapidly in the outflow and all carbonates became temporarily undersaturated, while zeolites became more saturated and Mg-saponite more supersaturated along with Fe-saponite. Comparable observations were also reflected in the reactive transport model.

The sequence of carbonate and clay saturation in this experimental study was dependent on pCO_2 and pH. The Fe-rich carbonates were stable at the highest pCO_2 and the Ca-rich carbonates at the lowest pCO_2. This is in agreement with observations from low temperature natural analogues in basaltic terrains (Rogers et al., 2006), the pure CO_2 phase of the CarbFix field injection site (Snæbjörnsdóttir et al., 2017), and our study's reactive transport model of the experiment. Similarly to CarbFix, the high molar volume Mg-saponite was undersaturated throughout the CO_2 laboratory injection once pH stabilized below 6. Fe- and Mg-saponites became supersaturated when the CO_2 injection was terminated and pH rose to about 8, while again confirmed by the reactive transport model though only Fe-saponite briefly formed when CO_2 injection began the second time.

Thus, during CO_2 injection into basaltic rocks one should aim at sufficiently low pH to start carbonate mineralization at the lowest possible pH to maximize the use of divalent cations for carbonization and create porosity near the injection well. Siderite saturation would therefore be at the center of the plume (*i.e.* injection of CO_2-charged fluid), followed by the sequence of Fe-, Mg-, and finally Ca-carbonates in the most dilute edges of the "plume" at the lowest pCO_2 and highest pH. This low pH carbonation has been referred to as the "sweet spot" of efficient carbonation (Snæbjörnsdóttir et al., 2018).

Discontinuous injection will always occur during industrial-scale carbon capture and storage due to equipment failure and/or overall service breaks. This experiment shows rapid alteration in the mineral saturation stages when CO_2 injection is terminated. Saturation states of large molar volume clays and zeolites increases along with one of the Ca-carbonates (calcite), while Fe-carbonates' saturation state decreases. Therefore for efficient use of the pore space in the subsurface during carbon storage, service breaks should be kept at a minimum during injection.

Acknowledgements

This publication has been produced with support from the European Commission through the projects CarbFix (EC Project 283148), CO2-React (EC Project 317235), and S4CE (EC Project 764810). The authors would like to thank editor Charles Jenkins for handling the manuscript and to the anonymous reviewers for their constructive comments that helped improve the manuscript. Special thanks to Giulia Alessandrini for her indispensable assistance in running the experiment, Sydney Gunnarson for material preparation, and Þorsteinn Jónsson for preparing, setting up, and taking apart the column. We would also like to acknowledge Rebecca Neely and Tobias Linke for their help in the laboratory in addition to Eric Oelkers, Peter Rendel, and the CarbFix group for their support.

Appendix A. Supplementary data

Supplementary material related to this article can be found, in the online version, at doi:https://doi.org/10.1016/j.ijggc.2019.07.007.

References

Adeoye, J.T., Menefee, A.H., Xiong, W., Wells, R.K., Skemer, P., Giammar, D.E., Ellis, B.R., 2017. Effect of transport limitations and fluid properties on reaction products in fractures of unaltered and serpentinized basalt exposed to high pCO_2 fluids. Int. J. Greenh. Gas Control. 63, 310–320. https://doi.org/10.1016/j.ijggc.2017.06.003.

Alfredsson, H.A., Oelkers, E.H., Hardarsson, B.S., Franzson, H., Gunnlaugsson, E., Gislason, S.R., 2013. The geology and water chemistry of the Hellisheidi, SW-Iceland carbon storage site. Int. J. Greenh. Gas Control 12, 399–418. https://doi.org/10.1016/j.ijggc.2012.11.019.

Andreani, M., Luquot, L., Gouze, P., Godard, M., Hoisé, E., Gibert, B., 2009. Experimental Study of Carbon Sequestration Reactions Controlled by the Percolation of CO2-Rich Brine through Periodotites. Environ. Sci. Technol. 43, 1226–1231. https://doi.org/10.1021/es8018429.

Aradóttir, E.S.P., Sonnenthal, E.L., Björnsson, G., Jónsson, H., 2012. Multidimensional reactive transport modeling of CO_2 mineral sequestration in basalts at the Hellisheidi geothermal field. Iceland. Int. J. Greenhouse Gas Control 9, 24–40. https://doi.org/10.1016/j.ijggc.2012.02.006.

Beckingham, L.E., Mitnick, E.H., Steefel, C.I., Zhang, S., Voltolini, M., Swift, A.M., Yang, L., Cole, D.R., Sheets, J.M., Ajo-Franklin, J.B., DePaolo, D.J., Mito, S., Xue, Z., 2016. Evaluation of mineral reactive surface area estimates for prediction of reactivity of a multi-mineral sediment. Geochim. Cosmochim. Acta 188, 310–329. https://doi.org/10.1016/j.gca.2016.05.040.

Beckingham, L.E., Steefel, C.I., Swift, A.M., Voltolini, M., Yang, L., Anovitz, L.M., Sheets, J.M., Cole, D.R., Kneafsey, T.J., Mitnick, E.H., Zhang, S., Landrot, G., Ajo-Franklin, J.B., DePaolo, D.J., Mito, S., Xue, Z., 2017. Evaluation of accessible mineral surface areas for improved prediction of mineral reaction rates in porous media. Geochim. Cosmochim. Acta 205, 31–49. https://doi.org/10.1016/j.gca.2017.02.006.

Birle, J.D., Gibbs, G.V., Moore, P.B., Smith, J.V., 1968. Crystal structures of natural olivines. Am. Mineral. 53, 807–824.

Daval, D., 2018. Carbon Dioxide Sequestration Through Silicate Degradation and Carbon Mineralisation: Promises and Uncertainties. Npj Materials Degradation 2. https://doi.org/10.1038/s41529-018-0035-4.

Galeczka, I., Wolff-Boenisch, D., Jonsson, T., Sigfusson, B., Stefansson, A., Gislason, S.R., 2013. A novel high pressure column flow reactor for experimental studies of CO_2 mineral storage. Appl. Geochem. 30, 91–104. https://doi.org/10.1016/j.apgeochem.2012.08.010.

Galeczka, I., Wolff-Boenisch, D., Oelkers, E.H., Gislason, S.R., 2014. An experimental study of basaltic glass–H_2O–CO_2 interaction at 22 and 50°C: implications for

subsurface storage of CO_2. Geochim. Cosmochim. Acta. 126, 123–145. https://doi.org/10.1016/j.gca.2013.10.044.
Gislason, S.R., Oelkers, E.H., 2003. Mechanism, rates, and consequences of basaltic glass dissolution: II. An experimental study of the dissolution rates of basaltic glass as a function of pH and temperature. Geochim. Cosmochim. Acta 67, 3817–3832. https://doi.org/10.1016/s0016-7037(03)00176-5.
Gislason, S.R., Aradóttir, E.S., Oelkers, E.H., 2018. A brief history of CarbFix: challenges and victories of the project's pilot phase. Energy Procedia 146, 103–114. https://doi.org/10.1016/j.egypro.2018.07.014.
Gislason, S.R., Wolff-Boenisch, D., Stefansson, A., Oelkers, E.H., Gunnlaugsson, E., Sigurdardottir, H., Sigfusson, B., Broecker, W.S., Matter, J.M., Stute, M., 2010. Mineral sequestration of carbon dioxide in basalt: a pre-injection overview of the CarbFix project. Int. J. Greenh. Gas Control. 4, 537–545. https://doi.org/10.1016/j.ijggc.2009.11.013.
Gudbrandsson, S., Wolff-Boenisch, D., Gislason, S.R., Oelkers, E.H., 2011. An experimental study of crystalline basalt dissolution from 2≤pH≤11 and temperatures from 5 to 75°C. Geochim. Cosmochim. Acta 75, 5496–5509. https://doi.org/10.1016/j.gca.2011.06.035.
Gysi, A.P., 2017. Numerical simulations of CO_2 sequestration in basaltic rock formations: challenges for optimizing mineral-fluid reactions. Pure Appl. Chem. 89, 581–596. https://doi.org/10.1515/pac-2016-1016.
Gysi, A.P., Stefánsson, A., 2012a. Experiments and geochemical modeling of CO_2 sequestration during hydrothermal basalt alteration. Chem. Geol. 306-307, 10–28. https://doi.org/10.1016/j.chemgeo.2012.02.016.
Gysi, A.P., Stefánsson, A., 2012b. Mineralogical aspects of CO_2 sequestration during hydrothermal basalt alteration — an experimental study at 75 to 250°C and elevated pCO_2. Chem. Geol. 306-307, 146–159. https://doi.org/10.1016/j.chemgeo.2012.03.006.
Hellevang, H., Haile, B.G., Tetteh, A., 2017. Experimental study to better understand factors affecting the CO_2 mineral trapping potential of basalt. Greenh. Gases Sci. Technol. 7, 143–157. https://doi.org/10.1002/ghg.1619.
Kanakiya, S., Adam, L., Esteban, L., Rowe, M.C., Shane, P., 2017. Dissolution and secondary mineral precipitation in basalts due to reactions with carbonic acid. J. Geophys. Res. Solid Earth 122, 4312–4327. https://doi.org/10.1002/2017JB014019.
Khalibad, M.R., Axelsson, G., Gislason, S.R., 2008. Aquifer characterization with tracer test technique; permanent CO_2 sequestration into basalt, SW Iceland. Mineral. Mag. 72, 121–125. https://doi.org/10.1180/minmag.2008.072.1.121.
Luhmann, A.J., Tutolo, B.M., Bagley, B.C., Mildner, D.F.R., Seyfried, W.E., Saar, M.O., 2017a. Permeability, porosity, and mineral surface area changes in basalt cores induced by reactive transport of CO_2-rich brine. Water Resour. Res. 53, 1908–1927. https://doi.org/10.1002/2016WR019216.
Luhmann, A.J., Tutolo, B.M., Tan, C., Moskowitz, B.M., Saar, M.O., Seyfried, W.E., 2017b. Whole rock basalt alteration from CO_2-rich brine during flow-through experiments at 150 °C and 150 bar. Chem. Geol. 453, 92–110. https://doi.org/10.1016/j.chemgeo.2017.02.002.
Matter, J.M., Broecker, W.S., Gislason, S.R., Gunnlaugsson, E., Oelkers, E.H., Stute, M., Sigurdardóttir, H., Stefansson, A., Alfreðsson, H.A., Aradóttir, E.S., Axelsson, G., Sigfússon, B., Wolff-Boenisch, D., 2011. The CarbFix Pilot Project–Storing carbon dioxide in basalt. Energy Procedia 4, 5579–5585. https://doi.org/10.1016/j.egypro.2011.02.546.
Matter, J.M., Kelemen, P.B., 2009. Permanent storage of carbon dioxide in geological reservoirs by mineral carbonation. Nat. Geosci. 2, 837–841. https://doi.org/10.1038/ngeo683.
Matter, J.M., Stute, M., Snæbjörnsdóttir, S.Ó., Oelkers, E.H., Gislason, S.R., Aradóttir, E.S., Sigfusson, B., Gunnarsson, I., Sigurdardóttir, H., Gunnlaugsson, E., Axelsson, G., Alfredsson, H.A., Wolff-Boenisch, D., Mesfin, K., Fernandez de la, Reguera, Taya, D., Hall, J., Dideriksen, K., Broecker, W.S., 2016. Rapid carbon mineralization for permanent disposal of anthropogenic carbon dioxide emissions. Science 352, 1312–1314. https://doi.org/10.1126/science.aad8132.
Menefee, A.H., Giammar, D.E., Ellis, B.R., 2018. Permanent CO_2 trapping through localized and chemical gradient-driven basalt carbonation. Environ. Sci. Technol. https://doi.org/10.1021/acs.est.8b01814.
McGrail, B.P., Schaef, H.T., Spane, F.A., Cliff, J.B., Qafoku, O., Horner, J.A., Thompson, C.J., Owen, A.T., Sullivan, C.E., 2017. Field validation of supercritical CO_2 reactivity with basalts. Environ. Sci. Technol. Lett. 4, 6–10. https://doi.org/10.1021/acs.estlett.6b00387.
Neveu, M., Desch, S.J., Castillo-Rogez, J.C., 2017. Aqueous geochemistry in icy world interiors: Equilibrium fluid, rock, and gas compositions, and fate of antifreezes and radionuclides. Geochim. Cosmochim. Acta 212, 324–371. https://doi.org/10.1016/j.gca.2017.06.023.
Oelkers, E.H., Gislason, S.R., 2001. The mechanism, rates and consequences of basaltic glass dissolution: I. An experimental study of the dissolution rates of basaltic glass as a function of aqueous Al, Si and oxalic acid concentration at 25°C and pH = 3 and 11. Geochim. Cosmochim. Acta 65, 3671–3681. https://doi.org/10.1016/S0016-7037(01)00664-0.
Oelkers, E.H., Gislason, S.R., Matter, J., 2008. Mineral carbonation of CO_2. Elements 4, 333–337. https://doi.org/10.2113/gselements.4.5.333.
Parkhurst, D.L., Appelo, C.A.J., 1999. User's Guide to PHREEQC (Version 2) - a Computer Program for Speciation, Batch-reaction, One-dimensional Transport, and Inverse Geochemical Calculations, Water-resources Investigations Report. U.S. Department of the Interior.
Parkhurst, D.L., Appelo, C.A.J., 2013. Description of input and examples for PHREEQC version 3 - a computer program for speciation, batch-reaction, one-dimensional transport, and inverse geochemical calculations. In: Survey, U.S.G. (Ed.), Techniques and Methods, pp. 497.
Rendel, P.M., Wolff-Boenisch, D., Gavrieli, I., Ganor, J., 2018. A novel experiment system for the exploration of CO_2-water-rock intereactions under conditions relevant to CO_2 geological storage. Chem. Eng. J. 334, 1206–1213. https://doi.org/10.1016/j.cej.2017.11.067.
Rogers, K.L., Neuhoff, P.S., Pedersen, A.K., Bird, D.K., 2006. CO_2 metasomatism in a basalt-hosted petroleum reservoir, Nuussuaq, West Greenland. Lithos 92, 55–82. https://doi.org/10.1016/j.lithos.2006.04.002.
Rosenbauer, R.J., Thomas, B., Bischoff, J.L., Palandri, J., 2012. Carbon sequestration via reaction with basaltic rocks: geochemical modeling and experimental results. Geochim. Cosmochim. Acta 89, 116–133. https://doi.org/10.1016/j.gca.2012.04.042.
Schaef, H.T., McGrail, B.P., Owen, A.T., 2010. Carbonate mineralization of volcanic province basalts. Int. J. Greenh. Gas Control. 4, 249–261. https://doi.org/10.1016/j.ijggc.2009.10.009.
Schiffman, P., Fridleifsson, G.Ó., 1991. The smectite-chlorite transition in drillhole NJ-15, Nesjavellir geothermal field, Iceland: XRD, BSE and electron microprobe investigations. J. Metamorph. Geol. 9, 679–696. https://doi.org/10.1111/j.1525-1314.1991.tb00558.x.
Sigfusson, B., Gislason, S.R., Matter, J.M., Stute, M., Gunnlaugsson, E., Gunnarsson, I., Aradottir E.S.,, Sigurdardottir H., Mesfin, K., Alfredsson, H.A., Wolff-Boenisch, D., Arnarsson, M.T., Oelkers, E.H., 2015. Solving the carbon-dioxide buoyancy challenge: the design and field testing of a dissolved CO_2 injection system. Int. J. Greenh. Gas Control. 37, 213–219. https://doi.org/10.1016/j.ijggc.2015.02.022.
Snæbjörnsdóttir, S.Ó., Gislason, S.R., Galeczka, I.M., Oelkers, E.H., 2018. Reaction path modelling of in-situ mineralisation of CO_2 at the CarbFix site at Hellisheidi, SW-Iceland. Geochim. Cosmochim. Acta 220, 348–366. https://doi.org/10.1016/j.gca.2017.09.053.
Snæbjörnsdóttir, S.Ó., Oelkers, E.H., Mesfin, K., Aradóttir, E.S., Dideriksen, K., Gunnarsson, I., Gunnlaugsson, E., Matter, J.M., Stute, M., Gislason, S.R., 2017. The chemistry and saturation states of subsurface fluids during the in situ mineralisation of CO_2 and H_2S at the CarbFix site in SW-Iceland. Int. J. Greenh. Gas Control. 58, 87–102. https://doi.org/10.1016/j.ijggc.2017/01.007.
Stockmann, G.J., Shirokova, L.S., Pokrovsky, O.S., Benezeth, P., Bovet, N., Gislason, S.R., Oelkers, E.H., 2012. Does the presence of heterotrophic bacterium *Pseudomonas reactans* affect basaltic glass dissolution rates? Chem. Geol. 296-297, 1–18. https://doi.org/10.1016/j.chemgeo.2011.12.011.
Stockmann, G.J., Wolff-Boenisch, D., Bovet, N., Gislason, S.R., Oelkers, E.H., 2014. The role of silicate surfaces on calcite precipitation kinetics. Geochim. Cosmochim. Acta 135, 231–250. https://doi.org/10.1016/j.gca.2014.03.015.
Stockmann, G.J., Wolff-Boenisch, D., Gislason, S.R., Oelkers, E.H., 2011. Do carbonate precipitates affect dissolution kinetics? 1: basaltic glass. Chem. Geol. 284, 306–316. https://doi.org/10.1016/j.chemgeo.2011.03.010.
Stockmann, G.J., Wolff-Boenisch, D., Gislason, S.R., Oelkers, E.H., 2013. Do carbonate precipitates affect dissolution kinetics? 2: diopside. Chem. Geol. 337-338, 56–66. https://doi.org/10.1016/j.chemgeo/2012.11.014.
Voigt, M., Marieni, C., Clark, D.E., Gislason, S.R., Oelkers, E.H., 2018. Evaluation and refinement of thermodynamic databases for mineral carbonation. Energy Procedia 146, 81–91. https://doi.org/10.1016/j.egypro.2018.07.012.
Wolff-Boenisch, D., Galeczka, I.M., 2018. Flow-through reactor experiments on basalt-(sea)water-CO_2 reactions at 90°C and neutral pH. What happens to the basalt pore space under post-injection conditions? Int. J. Greenh. Gas Control. 68, 176–190. https://doi.org/10.1016/j.gca.2005.10.016.
Wolff-Boenisch, D., Galeczka, I.M., Mesfin, K.G., Gislason, S.R., 2016. A foray into false positive results in mineral dissolution and precipitation studies. Appl. Geochem. 71, 9–19. https://doi.org/10.1016/j.apgeochem.2016.05.011.
Wolff-Boenisch, D., Gislason, S.R., Oelkers, E.H., 2006. The effect of crystallinity on dissolution rates and CO_2 consumption capacity of silicates. Geochim. Cosmochim. Acta 70, 858–870. https://doi.org/10.1016/j.gca.2005.10.016.
Wolff-Boenisch, D., Wenau, S., Gislason, S.R., Oelkers, E.H., 2011. Dissolution of basalts and peridotite in seawater, in the presence of ligands, and CO_2: implications for mineral sequestration of carbon dioxide. Geochim. Cosmochim. Acta 75, 5510–5525. https://doi.org/10.1016/j.gca.2011.07.004.
Xiong, W., Wells, R.K., Horner, J.A., Schaef, H.T., Skemer, P.A., Giammar, D.E., 2018. CO_2Mineral Sequestration in Naturally Porous Basalt. Environ. Sci. Technol. Lett. 5, 142–147. https://doi.org/10.1021/acs.estlett.8b00047.
Xiong, W., Wells, R.K., Menefee, A.H., Skemer, P., Ellis, B.R., Giammar, D.E., 2017. CO_2 mineral trapping in fractured basalt. Int. J. Greenh. Gas Control. 66, 204–217. https://doi.org/10.1016/j.ijggc.2017.10.003.